Title
Quantitative Kelvin probe force microscopy of current-carrying devices

Journal
Applied Physics Letters, 102(8)

ISSN
0003-6951

Authors
Fuller, Elliot J
Pan, Deng
Corso, Brad L
et al.

Publication Date
2013-02-25

DOI
10.1063/1.4793480

Peer reviewed

Quantitative Kelvin probe force microscopy of current-carrying devices

Elliot J. Fuller, Deng Pan, Brad L. Corso, O. Tolga Gul, Jose R. Gomez, and Philip G. Collins

Citation: Applied Physics Letters **102**, 083503 (2013); doi: 10.1063/1.4793480
View online: http://dx.doi.org/10.1063/1.4793480
View Table of Contents: http://scitation.aip.org/content/aip/journal/apl/102/8?ver=pdfcov
Published by the AIP Publishing

Quantitative Kelvin probe force microscopy of current-carrying devices

Elliot J. Fuller, Deng Pan, Brad L. Corso, O. Tolga Gul, Jose R. Gomez, and Philip G. Collins[a)]
Department of Physics and Astronomy, University of California Irvine, Irvine, California 92697, USA

(Received 10 January 2013; accepted 11 February 2013; published online 25 February 2013)

Kelvin probe force microscopy (KPFM) should be a key tool for characterizing the device physics of nanoscale electronics because it can directly image electrostatic potentials. In practice, though, distant connective electrodes interfere with accurate KPFM potential measurements and compromise its applicability. A parameterized KPFM technique described here determines these influences empirically during imaging, so that accurate potential profiles can be deduced from arbitrary device geometries without additional modeling. The technique is demonstrated on current-carrying single-walled carbon nanotubes (SWNTs), directly resolving average resistances per unit length of 70 kΩ/μm in semimetallic SWNTs and 200 kΩ/μm in semiconducting SWNTs.
 [http://dx.doi.org/10.1063/1.4793480]

Kelvin probe force microscopy (KPFM)[1] measures surface potentials with nearly atomic resolution[2,3] and minimal sample perturbation. Therefore, KPFM should be an ideal tool for characterizing nanoscale electronic devices, especially in cases where the device physics of novel materials is poorly understood. However, a primary limitation of KPFM is long-range capacitive coupling between the scanning probe and distant regions of a surface.[1,4–6] This coupling allows large, distant electrodes to contribute to the potentials and potential gradients measured by KPFM and ascribed to the probe tip's location. This problem is particularly acute when probing low-carrier density semiconductors, oxides, or other nanomaterials. Historically, this capacitive coupling problem has limited most KPFM research to the measurement of contact potential differences, such as work function variations between dissimilar materials[4] or across *p-n* junctions.[5] Effective solutions to the coupling problem, on the other hand, would improve quantitative imaging so that KPFM could map potential distributions along current-carrying pathways in active devices. This goal is a most promising application for KPFM, since it would help determine the device physics of novel or nanostructured electronic materials like organic polymers, graphene, or silicon nanowires.[4,7]

Achieving this aim motivates the development of KPFM techniques that minimize the artifacts introduced by long-range electrostatic coupling. Experimentally, KPFM imaging can be improved by decreasing the time-averaged height of the oscillating probe cantilever[6] and by operating in a frequency-modulated mode (FM-KPFM). Both techniques help minimize the contributions from parasitic capacitances but cannot eliminate them. A mathematical consideration of the Kelvin probe potential $\Phi_{KP}(x,y)$, which for FM-KPFM is given by the weighted sum

$$\Phi_{\mathrm{KP}}(x,y) = \sum_{i=1}^{n} \alpha_i(x,y) V_i = \sum_{i=1}^{n} \frac{\partial^2 C_i/\partial z^2}{\sum_{j=1}^{n} \partial^2 C_j/\partial z^2} V_i, \qquad (1)$$

shows that every equipotential surface V_i influences Φ_{KP} through its mutual capacitance C_i to the probe. In ideal cases, the coupling of the probe to distant surfaces is insensitive to the probe's oscillation, so that $d^2C_i/dz^2 = 0$ for each term except the surface potential $V_{surface}$ immediately below the probe tip. In that special case, $\alpha_{surface} = 1$ and $\Phi_{KP} = V_{surface}$. More generally, other coupling coefficients α_i are nonzero, and Φ_{KP} is a weighted average of $V_{surface}$ and other potentials V_i interacting with the probe tip.

The KPFM literature includes many discussions of this problem, including the development of analytical and numerical models for calculating the relevant α_i (x,y) and reconstructing $V_{surface}$ from Φ_{KP}.[7–11] The combination of experimental data with electrostatic modeling can be very effective in simple geometries like semi-infinite *p-n* junctions.[5] This reconstruction is less effective in dense device layouts or wherever thin, semiconducting channels are biased by high-carrier-density electrodes. In those cases, α_i of the electrodes can be comparable to $\alpha_{surface}$ at distances of several hundred nm. The spatial variation of α_i compounds the problem, adding voltage artifacts and preventing quantitative surface potential measurements along a path of interest.[12–14] Furthermore, it is very difficult for modeling to account for surface traps, channel defects, and other device imperfections that sometimes play major roles in the performance of nanoscale devices.[15]

Here, we combine the best experimental practices with an additional, empirical technique that further eliminates interference from multiple connected electrodes, so that additional modeling is not required to correctly determine potential gradients in an active, biased device. The technique involves acquiring FM-KPFM images while sweeping each relevant V_i through small ranges at every pixel of interest. A semi-automated sequence of biases applied to source, drain, and/or gate electrodes generated a multi-parameter FM-KPFM image $\Phi_{KP}(x,y,V_i)$. Gradients $d\Phi_{KP}/dV_i$ within the data set effectively measure each $\alpha_i(x,y)$ and directly determine the spatially dependent, relative coupling capacitance between each electrode and the KPFM probe at each pixel. By determining $\alpha_i(x,y)$ over the entire surface, this technique parameterizes complex

[a)]Author to whom correspondence should be addressed: Electronic mail: collinsp@uci.edu.

device geometries and allows for the separation and quantification of electrode potentials contributing to Φ_{KP} (though it does not directly improve other aspects of imaging such as lateral resolution). By comparison, modeling $\alpha_i(x,y)$ in a tool such as COMSOL MULTIPHYSICS proved too resource-intensive for general use, especially since accurate models required movement of the probe relative to the surface at each pixel. Furthermore, the experimental technique automatically accounted for device defects and strongly interacting surface traps that could not be predicted *a priori*. This parameterized KPFM technique should prove effective in any conditions where charged surface species are immobile, such as at low temperatures or in vacuum, but it may be less suitable for ambient imaging.

To demonstrate the technique, we examined potential gradients along individual, current-carrying, single-walled carbon nanotubes (SWNTs) in three-terminal, field effect transistor (FET) geometries. SWNT devices are an excellent test case that have proven to be quite complex in past research.[12,13,16–23] Because of their extremely small diameters (1 nm) and low carrier densities (1 to 100 μm^{-1}), SWNT channels couple very weakly to KPFM probe tips[12] and some researchers have concluded that SWNT potential gradients are too small to image reliably.[13,16,22]

Devices in our study consisted of dilute SWNTs synthesized by chemical vapor deposition directly on 4″ p^{++} silicon wafers with 250 nm backgate oxides. Platinum source and drain electrodes were defined by optical lithography and deposited over the SWNTs to define single-SWNT FET devices similar to those described in previous studies.[12,16,24,25] Devices were mounted in a high-vacuum, cryogenic KPFM (JEOL JSPM-5200) and characterized at 10^{-7} Torr and 200 K to eliminate artifacts from the ambient environment.[24,25] The source, drain, and backgate potentials (V_S, V_D, and V_G, respectively) were each controlled by custom software that integrated external analog signals (National Instruments NI-6289) into the FM-KPFM imaging mode of the instrument. Conventional silicon cantilevers (MikroMasch ULTRASHARP NSC15) coated with a 10 nm Pt film were used with an AC modulation of 500 mV at 1 kHz. Surface potential and topography were measured simultaneously using a frequency demodulation and Kelvin force feedback scheme that is typical for KPFM.[1] Specifically, shifts in the cantilever frequency were demodulated by a phased locked loop, tracked using an external lock-in amplifier (Stanford Research Systems SRS 830), and then nulled by a feedback loop that controlled the Kelvin probe potential Φ_{KP}. The experimental setup, along with all of the relevant biases and probe tip capacitances, is depicted in Fig. 1. Additional technical details describing our combination of scanning probe imaging with multi-parameter biasing have been described previously for scanning gate microscopy.[24,25]

Multiple SWNT FETs were imaged under various bias conditions, with similar results from all defect-free SWNTs. To best demonstrate the parameterized FM-KPFM method, Figures 2–4 all depict data from a single SWNT device, a semimetallic SWNT having a diameter of 1.1 nm, a channel length of 2.1 μm, and a DC resistance of 370 kΩ. Fig. 2(a) shows topography and raw FM-KPFM surface potential measurements for three bias conditions. At every pixel, Φ_{KP} was measured for a small range of biases around $V_G = -1$ V and $V_S = 0$ V to determine $\alpha_G(x,y)$ and $\alpha_S(x,y)$, respectively. Similar variation of V_D occurred around V_D set points ranging from −1.5 to +1.5 V. Using slices from the full data set

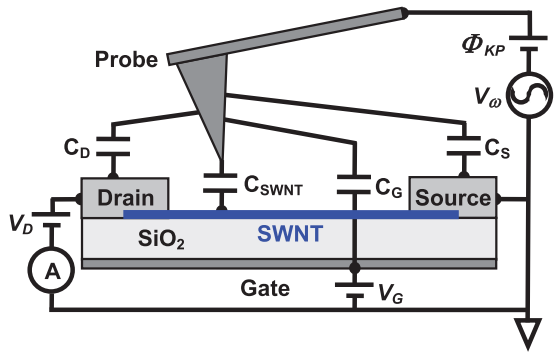

FIG. 1. Schematic of the FM-KPFM measurement technique and the capacitive couplings between the probe and each device electrode. Here, the conducting channel of interest is depicted as a SWNT FET.

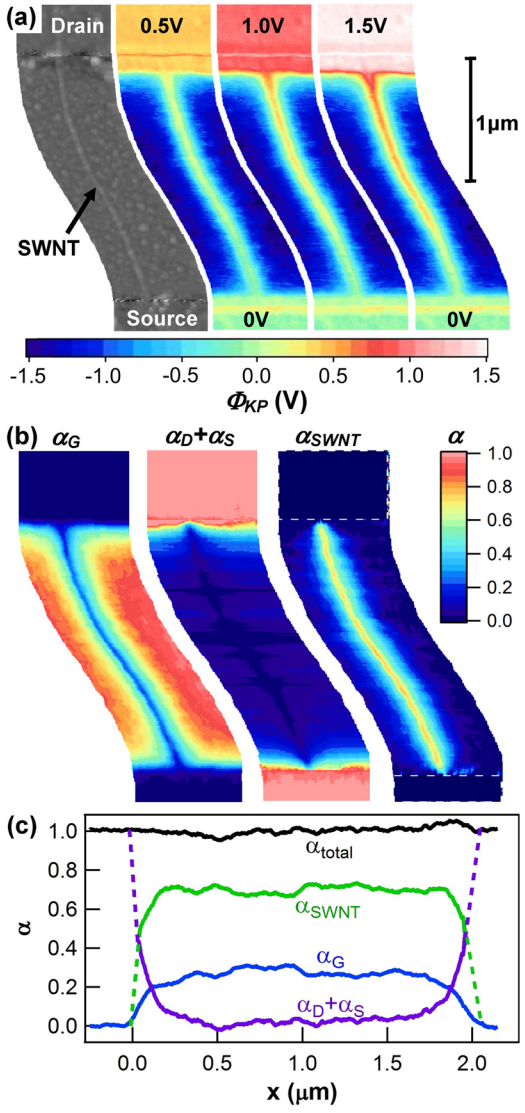

FIG. 2. (a) Topography (leftmost) and $\Phi_{KP}(x,y)$ for a SWNT device at three V_D biases, with Φ_{KP} depicted using a color scale. (b) Simultaneously measured weighting coefficients α for the backgate, drain and source electrodes, and SWNT channel. (c) Line cuts of $\alpha(x)$ following the SWNT channel ($0 > x > 2.1$ μm) and extending over source and drain electrode regions. A numerical sum of the α_i is also shown. Dashed lines indicate approximations in regions where the technique cannot fully separate α_{SWNT} from α_D or α_S.

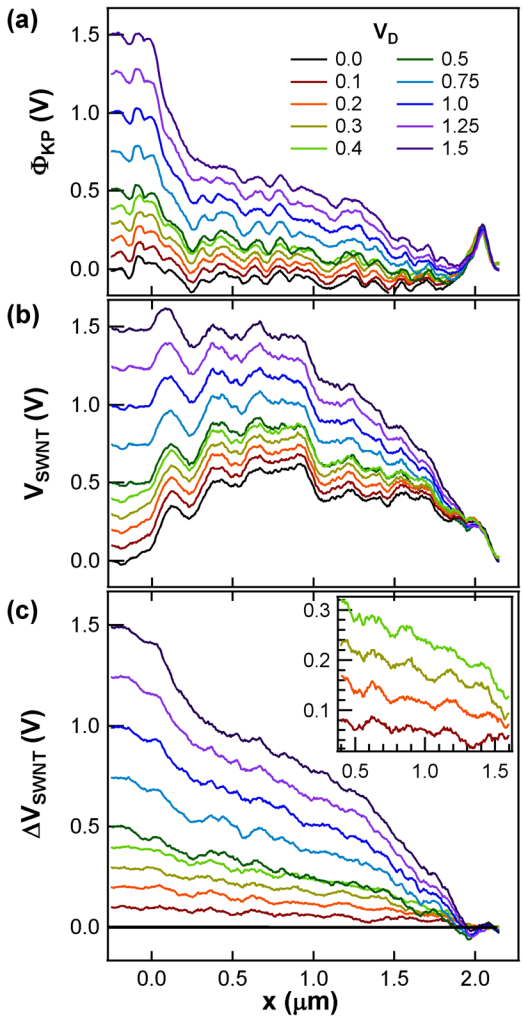

FIG. 3. (a) Line cuts of $\Phi_{KP}(x)$ taken directly over the SWNT at ten V_D biases. (b) The component of $\Phi_{KP}(x)$ due to surface potentials directly under the probe tip, as extracted from $\Phi_{KP}(x)$ using $\alpha_i(x)$ from Fig. 2. (c) After subtracting the $V_D = 0$ background variations, differential potentials highlight the true, dissipative potential drops along the SWNT. The inset shows low bias data at higher magnification.

$\Phi_{KP}(x,y,V_i)$, the derivatives $\alpha_G = d\Phi_{KP}/dV_G$ and $\alpha_D = d\Phi_{KP}/dV_D$ were determined over the entire surface.

Fig. 2(b) shows images of each α_i(x,y). Over the bare oxide, the probe coupled strongly to the gate electrode and

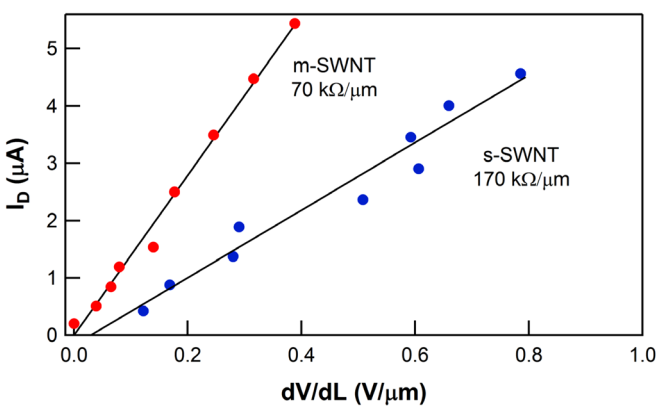

FIG. 4. Drain current versus average potential gradient for two types of SWNTs. A fit to each data set (solid lines) determines the average resistance per unit length, independent of any contact resistance.

α_G approached 1.0. Approaching the source or drain, α_G dropped to zero and these electrodes began to dominate the measured Φ_{KP}. The most important feature of the α images is not these average values but rather the empirical functional form of their spatial variation. For example, beginning from a value of 1 at the electrode edge, $\alpha_D(x)$ falls approximately as $e^{-x/L}$ with a characteristic length L = 140 nm. This rapid variation normally precludes quantitative KPFM analysis, since it causes spatial variation of Φ_{KP} even when the probe is over regions of uniform potential and work function.

Close to the SWNT, a third coefficient $\alpha_{SWNT}(x)$ couples the probe to the main potential of interest V_{SWNT}. V_{SWNT} is proportional to V_D, so the single derivative $d\Phi_{KP}/dV_D$ measured over the SWNT is a weighted combination of both α_{SWNT} and α_D. Nevertheless, data directly over the SWNT and parallel to the SWNT but displaced by 500 nm provides enough information to effectively separate the two contributions and produce the plot of α_{SWNT} shown in Fig. 2(b). At its maximum, α_{SWNT} averaged 0.7. This value is substantially larger than the 0.2 reported by Brunel *et al.*,[12] perhaps because of the increase in $\alpha_{surface}$ associated with the FM mode used here.[6] Directly over the SWNT and far from the electrodes, α_G averaged only 0.3 and we estimate that direct coupling to the distant source and drain electrodes contributed less than 3% to Φ_{KP}. Perpendicular to the SWNT, α_{SWNT} falls exponentially with nearly the same characteristic length L as at the electrode edge, indicating that the rapid growth of α_G dominates in both cases. Fig. 2(c) shows line cuts of each α_i directly along the SWNT and their sum α_{total}, which deviates less than ±5% from unity and confirms that all of the primary couplings have been accounted for.

Knowing each coupling factor $\alpha_i(x,y)$ makes it straightforward to isolate the desired surface potential from raw $\Phi_{KP}(x,y)$ data. Fig. 3 depicts this process by showing line cuts of $\Phi_{KP}(x,V_D)$ extracted along the SWNT [Fig. 3(a)] and the potential $V_{SWNT}(x,V_D)$ calculated using the spatially varying $\alpha_{SWNT}(x)$ [Fig. 3(b)]. In this data, $V_{SWNT}(x,V_D)$ is the more accurate potential measurement (lateral resolution of ~50 nm is limited by a finite tip radius, but independent techniques can further improve upon this aspect[9,11,23]). We note some of the important differences between $\Phi_{KP}(x,V_D)$ and V_{SWNT}. First, the flatness of $\Phi_{KP}(x,V_D = 0)$ has been interpreted in previous work on SWNTs as an indication that SWNT are quasi-ballistic, with minimal dissipative scattering. More correctly, $V_{SWNT}(x,V_D = 0)$ has a broad central maximum that is 0.4 to 0.6 V higher in potential than either end. This broad maximum is in better agreement with a bandstructure model, reflecting both a work function dissimilarity and the electrostatically induced carriers and band bending that result from the applied V_G. Second, we note a steep drop in $\Phi_{KP}(x,V_D = 1.5\text{ V})$ near the drain electrode that is typically ascribed to contact resistance at the SWNT-electrode interface. That drop vanishes in the corresponding $V_{SWNT}(x,V_D = 1.5\text{ V})$, proving that it actually results from the steep variations of $\alpha_i(x,y)$ that occur over $0 < x < 250$ nm.

Potential corrugations are observed along the SWNT in both $\Phi_{KP}(x,V_D)$ and $V_{SWNT}(x,V_D)$, and these are primarily caused by a fourth coupling term $\alpha_{oxide}V_{oxide}$. This term includes the weak but spatially varying contributions from charged surface contaminants, adsorbates, and traps in the

SiO_2, which are all relatively static in the low-temperature, vacuum environment used here. Previous research using scanning photocurrent microscopy has studied these traps, their optical excitations, and their effects on SWNT transport.[21] In KPFM, inhomogeneous point charges perturb $\Phi_{KP}(x,y)$ with a spatial dependence that is distinct from either α_{SWNT} or α_G and with virtually no dependence on V_D. These attributes allow the $\alpha_{oxide}V_{oxide}$ contribution to be easily separated and directly imaged when a wider range of V_G values are used. Here, no separation has been attempted, in part because the low-bias perturbations of point charges on SWNTs have been previously reported in detail.[17,18,21] As a result of their inclusion in the data, the $\alpha_{oxide}V_{oxide}$ contributions cause variations of the weighted couplings α_G and α_{SWNT} [Fig. 2(c)] and potential perturbations along the SWNT [Fig. 3(b)], even though the capacitive couplings d^2C_G/dz^2 and d^2C_{SWNT}/dz^2 are constant along the SWNT channel.

Rather than focusing on the perturbations caused by point charges, we instead focus on the V_D-dependent potential gradient along the SWNT channel. We subtract the background potential $V_{SWNT}(x,V_D=0)$ from every measurement of $V_{SWNT}(x,V_D\neq 0)$, thereby removing $\alpha_{oxide}V_{oxide}$ perturbations and highlighting the current-induced gradients caused by dissipative scattering, which are features of more general interest to the nanoscale device community.

Fig. 3(c) shows the resulting difference plots $\Delta V_{SWNT}(x,V_D)$, indicating the potential drops that occur when currents flow through the SWNT. Nine values of $V_D>0$ are shown in Fig. 3(c), and additional measurements at $V_D<0$ and with source and drain electrodes reversed were complementary. Overall, the $\Delta V_{SWNT}(x,V_D)$ curves are smooth and monotonic. Each curve has a wide, central region with a uniform slope, consistent with a constant scattering rate or resistance per unit length. This resistance per unit length is most clearly illustrated by plotting the mean slope $d\Delta V_{SWNT}/dx$ versus the current I_{sd} for each value of V_D, as shown in Fig. 4 (squares). The linear dependence indicates ohmic dissipation along the SWNT channel. The mean slope of 70 kΩ/μm corresponds to a mean free path of 90 nm, a channel resistance of 150 kΩ, and contact resistance of 220 kΩ. Identical experiments performed on a semiconducting SWNT observed a higher average resistivity of 170 kΩ/μm corresponding to a mean free path of 38 nm (Fig. 4, circles), a channel resistance of 545 kΩ, and a contact resistance of 55 kΩ.

These values are in excellent agreement with the SWNT transport literature,[26] particularly the finding of shorter scattering lengths in semiconducting SWNTs.[27] The notable aspect of this agreement is that FM-KPFM makes accurate and quantitative measurements accessible from a single device. Mean free path measurements typically require arrays of devices fabricated with different source-drain separations, so that scattering per unit length can be isolated from contact effects.[28,29] Quantitative FM-KPFM obtains the same information from short segments of a single device. Besides efficiency, this fact allows FM-KPFM to directly image anomalous resistances or device-specific behaviors,[30] including those which cannot be accounted for by scanned probe techniques that do not spatially resolve potential profiles.[31–33]

Closer to the drain and source electrodes, the $\Delta V_{SWNT}(x,V_D)$ curves in Fig. 3(c) become steeper. Contact resistance should, in fact, cause abrupt drops at the metal-SWNT interfaces, perhaps broadened by a combination of the KPFM lateral resolution and the extended depletion widths of SWNTs.[34] Unfortunately, these contact effects also occur in the regions where α_D and α_{SWNT} are most steeply varying and not fully separable. Additional investigation of these effects might benefit from measurements on devices having high contact resistances or gate-tunable Schottky barriers.

In conclusion, we have demonstrated a parameterized FM-KPFM technique that quantitatively measures surface potentials and resistivity along current-carrying nanodevices. The method does not rely on high aspect ratio tips or complex numerical simulations to reconstruct the potentials of interest, but rather removes artifacts empirically by directly measuring the coupling factors α_i and their spatial variation. The technique was demonstrated on isolated SWNTs as an extreme case of particularly weak coupling to the probe, but the technique is versatile enough for arbitrary device geometries and other electronic systems of similar complexity. The parameterized method can probably benefit any open- or closed-loop electrostatic imaging mode, including electrostatic force microscopy (EFM) and amplitude-modulated KPFM.

This work was supported financially by NSF (DMR-1104629).

[1]S. Sadewasser and T. Glatzel, *Kelvin Probe Force Microscopy: Measuring and Compensating Electrostatic Forces* (Springer, Berlin, 2012), p. 331.
[2]S. Kitamura and M. Iwatsuki, Appl. Phys. Lett. **72**, 3154 (1998).
[3]A. Sasahara, C. L. Pang, and H. Onishi, J. Phys. Chem. B **110**, 13453 (2006).
[4]H. O. Jacobs, P. Leuchtmann, O. J. Homan, and A. Stemmer, J. Appl. Phys. **84**, 1168 (1998).
[5]F. Robin, H. Jacobs, O. Homan, A. Stemmer, and W. Bachtold, Appl. Phys. Lett. **76**, 2907 (2000).
[6]U. Zerweck, C. Loppacher, T. Otto, S. Grafström, and L. Eng, Phys. Rev. B **71**, 125424 (2005).
[7]T. Hochwitz, A. K. Henning, C. Levey, C. Daghlian, and J. Slinkman, J. Vac. Sci. Technol. B **14**, 457 (1996).
[8]E. Strassburg, A. Boag, and Y. Rosenwaks, Rev. Sci. Instrum. **76**, 083705 (2005).
[9]A. Schwarzman, E. Grunbaum, E. Strassburg, E. Lepkifker, A. Boag, Y. Rosenwaks, T. Glatzel, Z. Barkay, M. Mazzer, and K. Barnham, J. Appl. Phys. **98**, 084310 (2005).
[10]T. Machleidt, E. Sparrer, D. Kapusi, and K. H. Franke, Meas. Sci. Technol. **20**, 084017 (2009).
[11]A. Liscio, E. Orgiu, J. M. Mativetsky, V. Palermo, and P. Samori, Adv. Mater. **22**, 5018 (2010).
[12]D. Brunel, D. Deresmes, and T. Mélin, Appl. Phys. Lett. **94**, 223508 (2009).
[13]Y. Miyato, K. Kobayashi, K. Matsushige, and H. Yamada, Nanotechnology **18**, 084008 (2007).
[14]Y.-J. Yu, Y. Zhao, S. Ryu, L. E. Brus, K. S. Kim, and P. Kim, Nano Lett. **9**, 3430 (2009).
[15]E. Koren, G. Elias, A. Boag, E. R. Hemesath, L. J. Lauhon, and Y. Rosenwaks, Nano Lett. **11**, 2499 (2011).
[16]A. Bachtold, M. S. Fuhrer, S. Plyasunov, M. Forero, E. H. Anderson, A. Zettl, and P. L. McEuen, Phys. Rev. Lett. **84**, 6082 (2000).
[17]M. T. Woodside and P. L. McEuen, Science **296**, 1098 (2002).
[18]M. Freitag, A. T. Johnson, S. V. Kalinin, and D. A. Bonnell, Phys. Rev. Lett. **89**, 216801 (2002).
[19]S. V. Kalinin, D. A. Bonnell, M. Freitag, and A. T. Johnson, Appl. Phys. Lett. **81**, 754 (2002).
[20]S. V. Kalinin, D. A. Bonnell, M. Freitag, and A. T. Johnson, Appl. Phys. Lett. **81**, 5219 (2002).

[21]M. Freitag, J. C. Tsang, A. Bol, P. Avouris, D. N. Yuan, and J. Liu, Appl. Phys. Lett. **91**, 031101 (2007).
[22]M. Ito, Y. Hosokawa, R. Nishi, Y. Miyato, K. Kobayashi, K. Matsushige, and H. Yamada, e-J. Surf. Sci. Nanotechnol. **9**, 210 (2011).
[23]M. Ito, K. Kobayashi, Y. Miyato, K. Matsushige, and H. Yamada, Appl. Phys. Lett. **102**, 013115 (2013).
[24]S. R. Hunt, D. Wan, V. R. Khalap, B. L. Corso, and P. G. Collins, Nano Lett. **11**, 1055 (2011).
[25]S. R. Hunt, E. J. Fuller, B. L. Corso, and P. G. Collins, Phys. Rev. B **85**, 235418 (2012).
[26]M. J. Biercuk, S. Ilani, C. M. Marcus, and P. L. McEuen, in *Carbon Nanotubes*, edited by A. Jorio, G. Dresselhaus, and M. S. Dresselhaus (Springer-Verlag, Berlin, 2008), Vol. 111, p. 455.
[27]P. L. McEuen, M. Bockrath, D. H. Cobden, Y. G. Yoon, and S. G. Louie, Phys. Rev. Lett. **83**, 5098 (1999).
[28]M. S. Purewal, B. H. Hong, A. Ravi, B. Chandra, J. Hone, and P. Kim, Phys. Rev. Lett. **98**, 186808 (2007).
[29]A. D. Franklin and Z. Chen, Nat. Nanotechnol. **5**, 858 (2010).
[30]A. D. Franklin, G. S. Tulevski, S.-J. Han, D. Shahrjerdi, Q. Cao, H.-Y. Chen, H. S. P. Wong, and W. Haensch, ACS Nano **6**, 1109 (2012).
[31]S. V. Kalinin and D. A. Bonnell, Appl. Phys. Lett. **78**, 1306 (2001).
[32]S. V. Kalinin and D. A. Bonnell, J. Appl. Phys. **91**, 832 (2002).
[33]X. Xie, K. L. Grosse, J. Song, C. Lu, S. Dunham, F. Du, A. E. Islam, Y. Li, Y. Zhang, E. Pop, Y. Huang, W. P. King, and J. A. Rogers, ACS Nano **6**, 10267 (2012).
[34]F. Leonard and J. Tersoff, Phys. Rev. Lett. **83**, 5174 (1999).